

# UC San Diego

## UC San Diego Previously Published Works

### Title

Cloud tomography applied to sky images: A virtual testbed

### Permalink

<https://escholarship.org/uc/item/9pg983d3>

### Authors

Mejia, Felipe A

Kurtz, Ben

Levis, Aviad

et al.

### Publication Date

2018-12-01

### DOI

10.1016/j.solener.2018.10.023

Peer reviewed

# Cloud tomography applied to sky images: A virtual testbed

Felipe A Mejia, Ben Kurtz, Aviad Levis, Íñigo de la Parra, Jan Kleissl

**Keywords:** 3D Cloud Reconstruction, Tomography, Cloud Optical Depth, Sky Imager, Solar Forecasting

Center for Renewable Resources and Integration, Department of Mechanical and Aerospace Engineering,  
University of California, San Diego 9500 Gilman Dr., La Jolla, CA 92093, USA

## Abstract

Two tomographic techniques are applied to two simulated sky images with different cloud fraction. The Algebraic Reconstruction Technique (ART) is applied to optical depth maps from sky images to reconstruct 3-D cloud extinction coefficients without considering multiple scattering effects. Reconstruction accuracy is explored for different products, including surface irradiance and extinction coefficients, as a function of the number of available sky imagers and setup distance. Increasing the number of imagers improves the accuracy of the 3-D reconstruction: for surface irradiance, the error decreases significantly up to four imagers at which point the improvements become marginal. But using nine imagers gives more robust results in practical situations in which the circumsolar region of images has to be excluded due to poor cloud detection. The ideal distance between imagers was also explored: for a cloud height of 1 km, increasing distance up to 3 km (the domain length) improved the 3-D reconstruction. An iterative reconstruction technique that iteratively updated the source function improved the results of the ART by minimizing the error between input red radiance images and reconstructed red radiance simulations. For the best case of a nine-imager deployment, the ART and iterative method resulted in 53.4% and 33.6% relative mean absolute error for the extinction coefficients, respectively.

## Nomenclature

### Abbreviations

AERONET	Aerosol Robotic Network
AirMSPI	Airborne Multi-angle SpectroPolarimetric Imager
ART	Algebraic reconstruction technique
CBH	Cloud base height
CF	Cloud fraction.
CTH	Cloud top height
DNI	Direct normal irradiance
GHI	Global horizontal irradiance
MAE	Mean absolute error
MBE	Mean bias error
MWR	Microwave radiometer
LES	Large eddy simulation

### Variables

$\mathcal{A}$	Matrix relating $k$ to $\tau_p$ [-]
$\mathbf{a}_p$	$p$ -th row of matrix $\mathcal{A}$ [-]
$f$	Focal length [m]
$I$	Radiance [ $\text{W} \cdot \text{sr}^{-1} \cdot \text{m}^{-2}$ ]
$I^{\text{meas}}$	Ground truth radiance from LES input into SHDOM [ $\text{W} \cdot \text{sr}^{-1} \cdot \text{m}^{-2}$ ]
$I_0$	Emitted radiance [ $\text{W} \cdot \text{sr}^{-1} \cdot \text{m}^{-2}$ ]
$i$	Gradient descent iterative step [-]
$J$	Source Function [ $\text{W} \cdot \text{m}^{-2} \cdot \text{sr}^{-1}$ ]
$j$	Iterative index [-]
$k$	Extinction coefficient [ $\text{m}^{-1}$ ]
$\mathbf{k}$	Matrix of all extinction coefficients in domain [-]
$\mathbf{k}^S$	Vector of extinction coefficients along a view path [-]

PB	Pixel brightness	$\mathbf{k}_{LES}$	Matrix of extinction coefficients from LES [-]
RRBR	Radiance Red-Blue Ratio	$L$	Distance between sky imagers [m]
SHDOM	Spherical harmonic discrete ordinate method	$LWC$	Liquid water content [ $\text{kg m}^{-3}$ ]
SI	Sky imagers	$m$	Index corresponding to the physical grid points [-]. $m = 1, \dots, N$
SZA	Solar zenith angle	$p$	Pixel index [-]. $p = 1, \dots, P$ , where P is the number of sky image pixels.
		$N_z$	Number of vertical levels in the domain [-]
		$r'$	Distance from the principal point in the image plane [m]
		$\mathbf{s}$	Position vector along the view path [m]
		$w$	Weighting factor [-]
		$\gamma$	Iterative step size [-]
		$\tau$	Optical path [m]
		$\tau_p$	Optical path for a particular pixel [m]
		$\mathcal{G}$	Zenith angle [ $^\circ$ ]
		$\mathcal{G}_p$	Zenith angle for a particular pixel [ $^\circ$ ]
		$\phi$	Azimuth [ $^\circ$ ]
		$\phi_p$	Azimuth for a particular pixel [ $^\circ$ ]
		$\theta$	Phase function [-]
		$\omega$	Single scattering albedo [-]
$\boldsymbol{\omega}_d$	Unit vector of direction [-]		

## 21 1. Introduction

22 The transition from conventional fossil energy to renewable energy has been aided by continued  
23 improvements in renewable technologies, but this progress is met with new challenges. Unlike conventional  
24 energy sources, which provide steady and reliable power output, solar energy generation requires larger  
25 regulation by ancillary generators to balance generation and demand during periods of high variability.  
26 Accurate forecasting of these periods of high variability will support management of the electric grid and  
27 electricity markets and, therefore, ensure a more economical integration of solar power (Mathiesen et al.,  
28 2013). Currently, several different methods are used to forecast at different spatial and temporal resolutions,  
29 including numerical weather prediction (Lorenz et al., 2009; Mathiesen and Kleissl, 2011) and satellite  
30 image-based forecasting (Hammer et al., 1999). Whole-sky imagery is the method of choice for short term  
31 forecasting (up to 15 minutes, e.g. Urquhart et al. (2013)). Physics-based solar forecasting using sky  
32 imagery (SI) has three main components: identifying clouds, advecting them, and calculating the solar  
33 energy that reaches the ground under the advected cloud field. Most algorithms assume that clouds exist as  
34 plane cloud at the cloud base height (CBH). In other words, the cloud geometric thickness is assumed to be  
35 negligible, which leads to projection errors (Kurtz et al., 2017). A perfect representation of the cloud field  
36 requires a 3-D matrix of cloud extinction coefficients  $\mathbf{k}(x,y,z)$  in the atmosphere.

37 Basic geometric cloud information has been derived in a few papers. CBH was obtained from stereography  
38 applied to two sky imagers by Nguyen and Kleissl (2014). Peng et al. (2015) expanded on this concept by  
39 providing a variable CBH for different cloud layers using multiple cameras but still assumed a negligible  
40 cloud geometric thickness. Cloud top height (CTH) was obtained from satellite data in Moroney et al.  
41 (2002). Although CBH and CTH are important aspects of the 3-D geometric description of a cloud, they do  
42 not completely describe the cloud properties. The cloud voxel technique in Oberländer et al. (2015) provides  
43 3-D cloud shape but does not provide extinction coefficients within the cloud; therefore it is not possible to  
44 calculate the resulting radiance field from first physical principles.

45 Tomography techniques have already been used to obtain 3-D atmospheric water vapor distribution from  
46 ground-based GPS observations (Wu et al., 2017; Ye et al., 2016). When it comes to completely describing  
47 cloud optical properties through 3D cloud extinction coefficients, stereography is insufficient as it only  
48 consists of taking two different camera views of a scene and reconstructing limited 3D information (such  
49 as CBH). On the other hand, in tomography a large number of measurements of the absorption of a scene  
50 are taken and used to fully reconstruct a scene in three dimensions, typically including the details inside of  
51 objects. Cloud tomography with sky imagers has been limited by the fact that most deployments only  
52 include three or less sky imagers and that sky imagers do not directly measure cloud absorption. These  
53 limitations are addressed in this paper as follows: (i) Up to 9 virtual sky imagers are “deployed” in a virtual  
54 cloud scene. (ii) The Radiance Red Blue Ratio (RRBR) technique (Mejia et al. 2017) yields optical depth  
55 from sky images enabling tomography using sky imagers.

56 Huang et al. (2008) applied tomography techniques to clouds using microwave radiometers, measuring line  
57 integrals of cloud emission along many directions. In optical wavelengths Levis et al. (2015) applied an  
58 iterative tomographic technique, minimizing the error between simulated and acquired images of the  
59 Airborne Multi-angle SpectroPolarimetric Imager (AirMSPI). Iterations are necessary to deal with the  
60 multiple scattering nature of light, however, it is time consuming. Aides et al. (2013) and Holodovsky et al.  
61 (2016) applied a sky-imagery tomographic approach for meteorological applications. This work, however,  
62 is motivated by real-time solar forecasting. To speed up reconstruction time, we rely on a fast algebraic  
63 reconstruction (Gordon et al., 1970) for initialization of the atmospheric extinction state (Section 2.2). This  
64 “initial guess” is subsequently improved with several iterations of the iterative approach (Section 2.3)  
65 allowing us to get the best of both worlds - speed and accuracy. This is the first time tomographic techniques  
66 are considered for solar forecasting, breaking free of the flat-plane paradigm (Chow et al., 2011) by  
67 capturing the full 3D effects of clouds. The testing layout is described in Section 3. Section 4 presents  
68 synthetic sky images reconstruction results and a cloud fraction sensitivity analysis. Section 5 presents  
69 discussion and conclusions.

## 70 **2. 3-D Reconstruction Methodology**

### 71 **2.1 Basic Principle**

72 To uniquely define a 3-D cloud scene, we need to know the extinction coefficients ( $k$ ) throughout the cloud  
73 scene. Similar problems exist in medical imaging, archaeology and generally in remote sensing and are  
74 known as computed tomography (Seeram, 2015). To solve for  $k$ , tomographic techniques relate  
75 measurements of transmission  $I/I_0$  to  $k$  as,

$$76 \quad I/I_0 = e^{-\int k(s)ds} = e^{-\tau}, \quad (1)$$

77 where  $I$  is the transmitted or attenuated radiance,  $I_0$  is the emitted radiance (from the sun),  $s$  is the path  
78 along the beam, and  $\tau$  is the line integral of  $\mathbf{k}$  or optical path. The steady and collimated sun is a  
79 homogeneous radiation source. With multiple transmission measurements at different orientations, the  
80 extinction coefficients can be determined. For cloud tomography, we solve for  $\mathbf{k}$  of the 3-D cloud field  
81 from measurements of  $I$  by multiple sky imagers.

## 82 **2.2. Algebraic Reconstruction Technique**

83 Discretizing the domain with the tomography problem stated in Eq.(1) yields the following matrix equation:

$$84 \quad \mathcal{A}\mathbf{k} = \boldsymbol{\tau}. \quad (2)$$

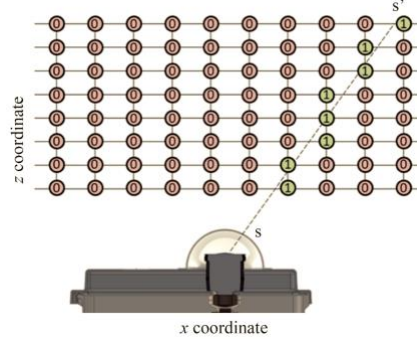
85 Here, the vector of extinction coefficients  $\mathbf{k} = (k_1, k_2, \dots, k_n)$  is the solution to be obtained by solving the  
86 system of linear equations. Although  $\mathbf{k}$  represents extinction coefficients on a 3-D physical grid, for  
87 notational conciseness we will use it here as a vector, so  $N = (N_x \times N_y \times N_z)$  is the number of grid points  
88 in the domain.  $\boldsymbol{\tau}$  is the vector of measurements of optical path, so for applications with sky imagers it is  
89 derived from the Radiance Red Blue Ratio (RRBR) method (Mejia et al., 2016). The RRBR method uses a  
90 look-up table created from homogenous (overcast) cloud images to estimate  $\tau_p$  for each pixel in each sky  
91 image.  $\boldsymbol{\tau}$  then consists of  $P = \sum_i P_i$  elements representing all pixels from all sky imagers. Where we need  
92 to express the direction represented by a particular sky image, we will denote the pixel zenith angle (or  
93 view angle) as  $\mathcal{G}_p$  and the azimuth as  $\phi_p$ .

94 We further approximate the line integrals (now represented by matrix multiplication) by assuming that only  
95 one grid cell contributes at each  $z$  level in the physical grid, such that  $\mathcal{A}$  is a matrix with ones when the  
96 element  $\mathcal{A}_{p,m}$  satisfies the following equalities:

$$97 \quad x_{p,m} = \text{nearest}(z_m \tan(\mathcal{G}_p) \sin(\phi_p) + x_{si}) \quad (3)$$

$$98 \quad y_{p,m} = \text{nearest}(z_m \tan(\mathcal{G}_p) \cos(\phi_p) + x_{si}), \quad (4)$$

100 and  $\mathcal{A}_{p,m} = 0$  elsewhere.  $m = 1, \dots, N_z$  is the index corresponding to the physical grid points,  $z_m$  is the  $z$   
101 coordinate of the grid point relative to the SI elevation, and  $x_{si}$  and  $y_{si}$  are the horizontal coordinates of the  
102 SI location for measurement  $p$ . In the equations ‘nearest (...)’ represents rounding to the nearest grid  
103 coordinate. In this way,  $\mathcal{A}$  is a sparse matrix that substantially reduces the computational cost of solving  
104 the system of equations. An example slice of matrix  $\mathcal{A}$  obtained from applying Eqs. (3) and (4) is  
105 demonstrated in Figure 1 for one SI pixel.



106

107 Figure 1. Conceptual diagram of ray tracing to create matrix  $\mathcal{A}$  in Eq. 2 for one SI pixel along the view path  $s$ .  $\mathcal{A}$  is a 3-D matrix,  
 108 but here only a vertical slice in  $x$ - $z$  is shown. Numbers in the circles denote the values of  $\mathcal{A}$ .

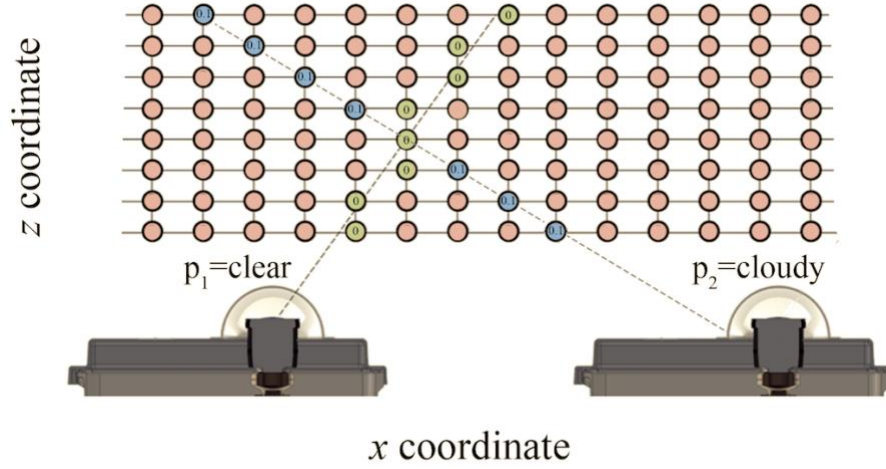
109 To solve the system of equations in Eq. 2, we will use the algebraic reconstruction technique (ART) of  
 110 Gordon et al., (1970). ART is a family of algorithms to reconstruct  $\mathbf{k}$  by solving a system of linear  
 111 equations. The conventional ART method iteratively adjusts  $\mathbf{k}^s$  (the extinction coefficient vector along a  
 112 view path  $s$  associated with pixel  $p$ ) as,

$$113 \quad \mathbf{k}_j^s = \mathbf{k}_{j-1}^s + \frac{\tau_p - \mathbf{a}_p \cdot \mathbf{k}}{\|\mathbf{a}_p\|^2} \mathbf{a}_p, \quad (5)$$

114 where  $\mathbf{a}_p$  is the  $p$ -th row of the matrix  $\mathcal{A}$ , which maps one pixel in an image to the  $\mathbf{k}^s$  along its view path,  
 115 and  $j$  is the iterative index. Our implementation slightly differs by iteratively adjusting  $\mathbf{k}^s$  as,

$$116 \quad \mathbf{k}_j^s = \mathbf{k}_{j-1}^s \left[ 1 + w \left( \frac{\tau_p}{\mathbf{a}_p \cdot \mathbf{k}} - 1 \right) \right], \quad (6)$$

117 where  $w$  is a weighting factor that is empirically set to 0.2. Eq. 6 is preferred over Eq. 5 as it naturally  
 118 preserves clear grid points ( $k_m = 0$ ), and avoids negative values in  $\mathbf{k}$  as opposed to the original ART  
 119 method. Eq. 6 is first applied to all pixels of one sky imager ( $p = 1, \dots, P_i$ ), then sequentially to the other  
 120 sky imagers, and then  $j$  increments by one and the process repeats until convergence. The 3-D  $\mathbf{k}$  matrix is  
 121 continually updated with the solutions  $\mathbf{k}_j^s$ . The solution  $\mathbf{k}_j^s$  is further constrained by requiring  $\mathbf{k}_j^s = 0$  when  
 122  $\tau_p = 0$  consistent with Oberlander et al. (2015), which ensures more accurate solutions with less  
 123 computational effort. When a pixel in a different sky imager is considered, the elements of  $\mathbf{k}$  that were  
 124 already marked as clear by another sky imager will not be included in the ART update of  $\mathbf{k}$  (Figure 2). This  
 125 constraint is equivalent to geometrical space-carving (Veikherman et al., 2015).



126

127 Figure 2: Conceptual diagram of ray tracing to create matrix  $\mathbf{k}$  in Eq. 2 for two SI pixel along two view paths. The left sky  
 128 imager pixel  $p_1$  shows clear skies and all extinction coefficients along the associated view path are set to zero. The right sky  
 129 imager shows a cloud in pixel  $p_2$  and (initially) constant extinction coefficients are introduced along the associated view path,  
 130 except along known clear grid points.  $\mathbf{k}^s$  elements of 0.1 are chosen randomly here.

131

### 132 2.3. Iterative Retrieval

133 The ART method does not directly account for the effects of 3-D scattering. Therefore, non-local effects  
 134 leading to adjustment of the extinction coefficients are unaccounted for. To improve the ART results, the  
 135 iterative approach developed by Levis et al. (2015) for satellite data is implemented for sky images. After  
 136 initializing  $\mathbf{k}$  with the ART, the domain is simulated in a radiative transfer model. A gradient descent is  
 137 applied iteratively to  $\mathbf{k}$  to minimize the difference between measured transmitted radiance  $I^{\text{meas}}$  and the  
 138 transmitted radiance simulated by Spherical Harmonic Discrete Ordinate Method (SHDOM),  $I$  (Aides et  
 139 al., 2013; Levis et al., 2017; Veikherman et al., 2015).

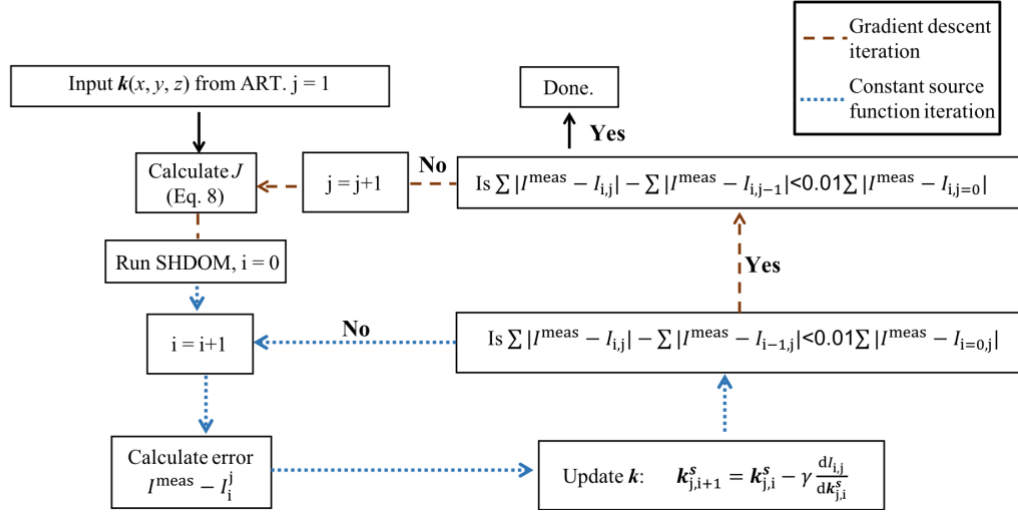
140 As background consider the integral form of the radiative transfer equation,

$$141 \quad I(s, \boldsymbol{\omega}_d) = \exp\left[-\int_0^s \mathbf{k}(s') ds'\right] I((x_{s_1}, y_{s_1}), \boldsymbol{\omega}_d) + \int_0^s \exp\left[-\int_s^t \mathbf{k}(t) dt\right] J(s', \boldsymbol{\omega}_d) \mathbf{k}(s') ds', \quad (7)$$

142 where  $I((x_{s_1}, y_{s_1}), \boldsymbol{\omega}_d)$  is extraterrestrial radiance at a ground location  $(x_{s_1}, y_{s_1})$  incident from direction  
 143  $\boldsymbol{\omega}_d$ ,  $\int_s^{s'} \mathbf{k}(t) dt$  is a line integral over a field  $\mathbf{k}$  along the segment extending from  $s$  to  $s'$  illustrated as the  
 144 dashed line in Figure 1,  $\boldsymbol{\omega}_d$  is the unit vector representing the direction of the view path,  $t$  is a dummy  
 145 variable for integration, and  $J$  is the source function, which contributes the non-local scattering effects.  
 146 Neglecting emission from the cloud, the source function  $J$  is

$$147 \quad J(s, \boldsymbol{\omega}_d) = \frac{\omega}{4\pi} \int_0^{4\pi} I(s, \boldsymbol{\omega}'_d) \theta(s; \boldsymbol{\omega}_d, \boldsymbol{\omega}'_d) d\boldsymbol{\omega}'_d, \quad (8)$$

148 where  $\omega$  is the single scattering albedo and  $\theta(\mathbf{s}; \omega_d, \omega'_d)$  is the phase function at  $s$ . The phase function  
 149 describes the fraction of energy scattered from  $\omega'_d$  to  $\omega_d$  by an infinitesimal volume (Levis et al., 2015).  
 150 Eq. 7 shows that  $I$  explicitly depends on  $\mathbf{k}$  along the view path. When discretized,  $I$  then only depends on  
 151 the  $\mathbf{k}$  located along that  $I$  view path as illustrated in Figure 1. This integral of  $\mathbf{k}$  in Eq. 7 is easily iterated to  
 152 minimize  $I^{\text{meas}} - I$  (described in Eq. 9 below), but  $J$  causes the iterative process for one direction to depend  
 153 on the iterations at all other angles through 3-D scattering effects.  $I$  also implicitly depends on  $\mathbf{k}$  through  $J$ ,  
 154 because scattering anywhere in the domain can increase  $J$  at a particular view path.  $J$  depends on the  $I$  in all  
 155 directions such that iterating neighboring pixels affect all other pixels due to multiple scattering of radiation  
 156 within and between clouds.



157

158 Figure 3. Flow chart of the iterative retrieval method. Dotted and dashed arrows correspond to constant source function and  
 159 gradient descent iterations, respectively.

160 Figure 3 demonstrates the flow chart of the implementation of this iterative method. Since a more accurate  
 161 initialization decreases the computational cost,  $\mathbf{k}$  from the ART method is input to the iterative method. In  
 162 the inner loop optimization (dotted arrows) a constant  $J$  is assumed. Then  $I^{\text{meas}} - I$  is minimized iteratively  
 163 by adjusting  $\mathbf{k}$  at the grid points along  $s$  following a gradient descent method as

$$164 \quad \mathbf{k}_{j,i+1}^s = \mathbf{k}_{j,i}^s - \gamma \frac{dI_{i,j}}{dk_{j,i}^s}, \quad (9)$$

165 where  $j$  is the constant source function iterative step,  $i$  is the gradient descent iterative step, and  $\gamma$  is the  
 166 step size. Eq. 9 is repeated for all pixels in a sky image ( $p = 1, \dots, P_i$ ), and then for all sky imagers, and this  
 167 is repeated until convergence. Convergence is met when the change in the total image error is less than 1%  
 168 of the original error following

$$169 \quad \sum |I^{\text{meas}} - I_{i,j}| - \sum |I^{\text{meas}} - I_{i-1,j}| < 0.01 \sum |I^{\text{meas}} - I_{i=0,j}|, \quad (10)$$

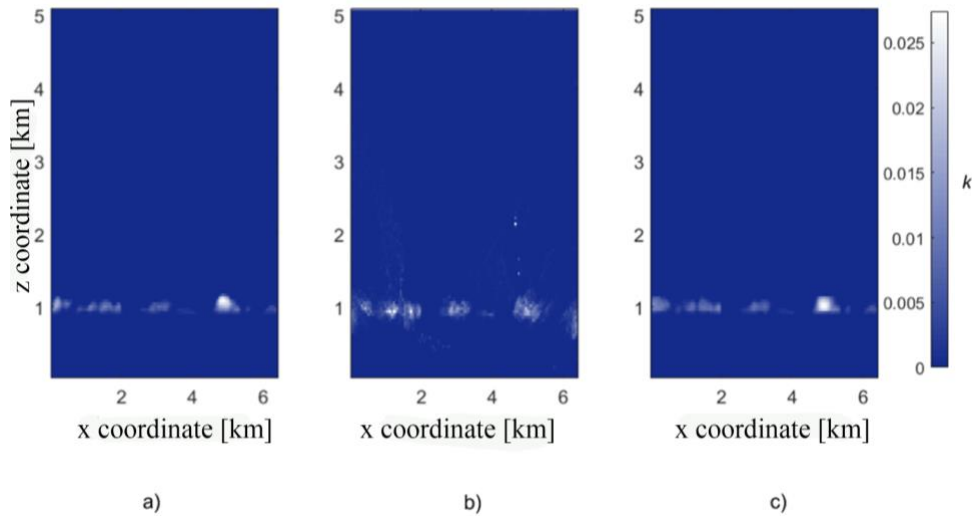
170 where  $\sum$  represents summation over all pixels in all images. Once Eq. 10 is satisfied, we recalculate  $J$  (and  
 171 repeat the inner loop) until the change in the total image error decreases to 1% of the original error:

$$172 \quad \sum |I^{\text{meas}} - I_{i,j}| - \sum |I^{\text{meas}} - I_{i,j-1}| < 0.01 \sum |I^{\text{meas}} - I_{i,j=0}|. \quad (11)$$



173 **2.4. Constraining Cloud Base and Cloud Top Height**

174 Two critical pieces of information obtained from cloud reconstruction are the CBH and CTH (Sun et al.,  
175 2016; Wang et al., 2016). Figure 4a shows one of the cloud scenes with a CTH of 1.2 km, a CBH of 820 m  
176 and Figure 4b and c show the ART results. Cloud artifacts are erroneously reconstructed below and above  
177 the real cloud layer, for example at  $x = 1.5$  km and  $x = 4.3$  km in the unconstrained ART method in Figure  
178 4b. In general, artifacts occur because Eq. 6 is ill-conditioned due to a lack of different perspectives for  
179 some points. A lack of different perspectives can result from large CBH relative to the imager spacing  $L$ ,  
180 i.e. large  $CBH / L$ . If none of the imagers ‘sees’ the air immediately above the cloud, the reconstruction  
181 lacks sufficient information to clear these areas of clouds resulting in vertical lines or cones in the  
182 reconstructed image. To remove these artifacts, we assume that no clouds are present 250 m below the CBH  
183 or 250 m above the CTH (Figure 4c). The CBH and CTH are the heights of the highest and lowest non-  
184 zero extinction coefficients found in the large eddy simulation (LES) scenes. The CBH and CTH  
185 information used here is known a priori in this case, but might not be available in real life cases. Ceilometers  
186 can determine CBH with an accuracy better than 250 m. Estimating CTH in practice is more challenging,  
187 however CTH (and CBH) could be estimated with temperature and humidity profiles from radiosondes  
188 (Zhong et al., 2017).



189 a) b) c)  
190 Figure 4. 2-D slice through  $k$  averaged along the  $y$ -axis from a) Large Eddy Simulation (LES); b) Reconstruction with 9 sky imagers  
191 separated by 1.5 km using the Algebraic Reconstruction Technique (ART) method; and c) improved reconstruction with cloud base  
192 and top height constraints.

193 **3. Testing Layout**

194 **3.1. Objective and Domain Size**

195 The objective is to reconstruct the 3D extinction coefficient  $k(x,y,z)$  within a solar forecast domain from  
196 sky images. The improved accuracy of the initial state is expected to result in more accurate short-term  
197 forecasts. Sky imagers can provide valuable solar forecast information up to 15 min ahead depending on  
198 cloud speed, cloud height, and cloud dynamics (Chow et al., 2015; Martín and Trapero, 2015; Quesada-  
199 Ruiz et al., 2014; Schmidt et al., 2015; Sun et al., 2016). Given that cloud speeds from the LES described

200 in Section 3.2 vary between 8 to 10 m/s, domains should be on the order of 8 km (= 15 min × 9 m/s = 8.1  
201 km). We chose a cloud domain of 6.4 by 6.4 km horizontal and 5 km vertical size with 50 m horizontal and  
202 40 m vertical resolution for a total of 2,080,768  $k$  points.

203 Perfect 3D reconstruction requires that all sky imager cameras are geometrically and photometrically  
204 calibrated. Geometric calibration ensures accurate georeferencing of view paths for a single imager and for  
205 a cloud or clear space observed by two imagers and techniques for accurate in-situ geometric calibration  
206 exist (Urquhart et al., 2016). Photometric calibrations ensure that red-green-blue pixel brightnesses are  
207 uniquely and accurately converted to optical depths. We acknowledge that in practice sky imagers are rarely  
208 photometrically calibrated in an absolute sense (the only known evaluation of photometric properties is  
209 presented in Urquhart et al. (2015)). But as long as sky imagers are photometrically calibrated *relative* to  
210 each other, the reconstruction could be used to derive relative extinction coefficients from sky imagers and  
211 geometrically constrain clouds. Since all radiances at the ground depend linearly on the incident radiation  
212 at the top of the reconstruction domain, measurements from a single calibrated pyranometer in the domain  
213 could then be used for absolute calibration of the extinction coefficients.

214 Another objective is to investigate the sensitivity of the tomographic techniques to different deployment  
215 configuration variables, specifically the number of imagers and the distance between imagers. It is expected  
216 that the reconstruction accuracy improves with more imagers, but at the expense of acquisition, setup, and  
217 maintenance of additional equipment. Therefore, if additional improvements are marginal, fewer sky  
218 imagers would be preferred. The sensitivity to cloud fraction is also examined. Unless they are near zenith  
219 of a sky image, even clouds in a single cloud layer can block the views of other clouds behind them and  
220 deteriorate reconstruction accuracy. In the extreme case of overcast conditions, 3D reconstruction would  
221 become impossible as no image information of the cloud top is available.

222 The sensitivity study would be compromised by  $\tau_p$  errors in the RRBR method which are used to assign  
223 cloud optical depth to each sky imager pixel and associated view path. For example, it is well documented  
224 that clouds are more difficult to detect in the circumsolar region (Yang et al., 2014) and that deployments  
225 with fewer clouds in the circumsolar region will perform better. For purposes of the sensitivity study, we  
226 therefore prevent random errors associated with the location of the clouds relative to the cameras by using  
227 a perfect  $\tau$  defined as

$$228 \quad \tau = \mathcal{A}k_{\text{LES}}. \tag{12}$$

### 229 **3.2. Virtual Cloud Fields and Sky Images**

230 The 3-D reconstruction methods are tested in the virtual testbed from Kurtz et al. (2017). This virtual testbed  
231 uses the University of California, Los Angeles (UCLA) LES (Stevens, 2010) to model a realistic 3-D  
232 atmospheric boundary layer with continental cumulus clouds at high resolution for a time period of 24  
233 hours. Periodic boundary conditions represent infinite domains with the same ground cover, which allows  
234 the cloud and atmospheric turbulence to spin up and create realistic cloud shapes and dynamics such as  
235 condensation, evaporation and deformation. From the LES run, 3D liquid water content (LWC) of two  
236 representative time instances (at 4:38 h and 6:57 h after initialization) with cloud fractions of 6.8% and  
237 33.3% are selected for reconstruction. Cloud fraction is defined as the fraction of grid points occupied by  
238 clouds in a vertical projection of the cloud field.

239 The LES LWC is input into the SHDOM (Evans, 1998) to produce radiance fields ( $I^{\text{meas}}$ ) at a constant  
240 solar zenith angle (SZA) of  $45^\circ$ . The SHDOM radiance field reproduces a  $1701 \times 1701$  pixel sky image as  
241 would be obtained through a fisheye lens with an equisolid angle projection (Miyamoto, 1964)

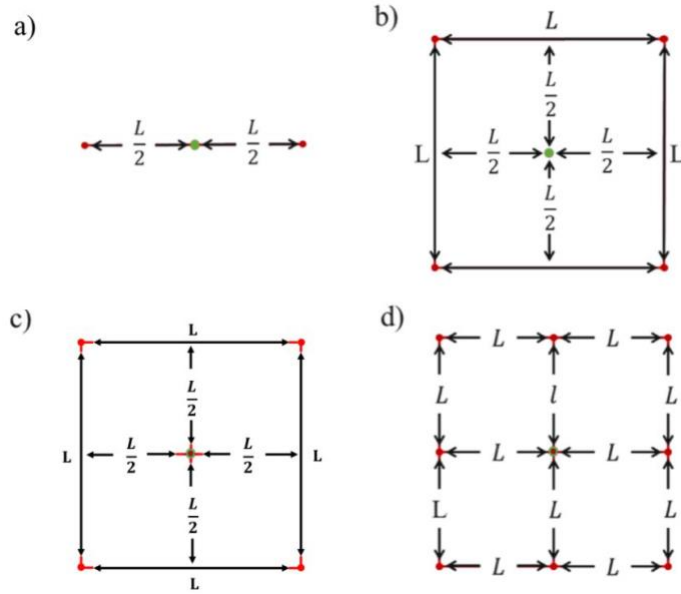
$$242 \quad r' = 2f \sin\left(\frac{\theta_p}{2}\right), \quad (13)$$

243 where  $f$  is the focal length, and  $r'$  is the distance from the principal point in the image plane. Three different  
244 wavelengths are simulated corresponding to the peak responses of the SI camera's red (620 nm), green (520  
245 nm) and blue (450 nm) channels. The aerosol phase function, background Rayleigh and aerosol optical  
246 depths are obtained from the yearly average Aerosol Robotic Network (AERONET) measurements (Holben  
247 et al., 1998) as in Mejia et al. (2016). Spectral surface reflectances of 0.043, 0.068, and 0.071 were used for  
248 the blue, green and red channel simulations, respectively (Markham, 1992; Mejia et al., 2016). The cloud  
249 droplet effective radius, which is the area weighted mean radius of the cloud droplets, is  $8 \mu\text{m}$  (Min, 2003)  
250 and defines the single scattering properties of the clouds in the SHDOM simulations. SHDOM simulations  
251 use open boundary conditions (Evans, 2015, 1998), which means that measurements outside the LES  
252 domain are not used for reconstruction.

### 253 **3.3. Sky Imager Deployment Layouts**

254 A sensitivity study elucidates the tradeoffs between different SI deployment variables, specifically the  
255 number and distance between imagers. A similar study by Huang et al. (2008) with MWR tomography  
256 found that the optimal number of MWR was 4, and that the optimal distance between MWR was 4 km.  
257 Nguyen and Kleissl (2014) demonstrated that the optimal distance between imagers for stereography is  
258 directly related to the CBH; therefore the optimal distance between imagers is expected to apply only for  
259 the CBH of our test case, which is 0.94 km.

260 To compare the tradeoffs of using multiple imagers, we simulated 2, 4, 5 and 9 imagers arranged as outlined  
261 in Figure 5. To obtain the optimal distance between imagers, we tested setups of 2, 4, 5 and 9 evenly spaced  
262 imagers symmetric to the center of the domain. Imagery are separated by distances  $L = [0.25 \ 0.5 \ 1.0 \ 1.5$   
263  $2.0 \ 3.0 \ 4.0 \ 6.0]$  km with a few exceptions: (i)  $L$  is restricted to 3.0 km for the 9 imager setup; (ii) To make  
264 it comparable to the 4 imager setup, for the 5 imager setup the 5<sup>th</sup> imager is located at the center of the  
265 square formed by the 4 imagers. The dependence of reconstruction errors on the optimal number of imagers  
266 was analyzed with the respective spacings that minimized reconstruction error.



267

268 Figure 5. Layout of sky imager deployments with different number of imagers and distance ( $L$ ) between imagers, a) 2 imagers  
 269 along the  $x$ -axis, b) 4 imagers, c) 5 imagers and d) 9 imagers. Red dots represent imager locations, and the green circle (green  
 270 outline when imager located at center of domain) represents the center of domain.

### 271 3.4. Error Metrics

272 Since measuring cloud properties of real clouds is extremely challenging, the main benefit of using  
 273 simulated test cases is the validation against spatially-resolved cloud properties. To this end, we are  
 274 interested in analyzing errors in extinction coefficient, image red (620 nm) pixel brightness (PB) and surface  
 275 Global Horizontal Irradiance (GHI). The red PB has been arbitrarily selected, however, any of the red,  
 276 green, blue channels could be used. While perfect  $k$  retrievals would automatically result in perfect image  
 277 PB and surface GHI, erroneous  $k$  retrievals may have different impacts on GHI and image errors, which  
 278 are more relevant in the practice of solar forecasting. We will quantify these errors by calculating the  
 279 domain relative mean absolute error (rMAE) and relative mean bias error (rMBE), defined as

$$280 \text{rMAE} = \frac{\overline{k_{\text{LES}} - k}}{k_{\text{LES}}}, \quad (14)$$

$$281 \text{rMBE} = \frac{\overline{k - k_{\text{LES}}}}{k_{\text{LES}}}, \quad (15)$$

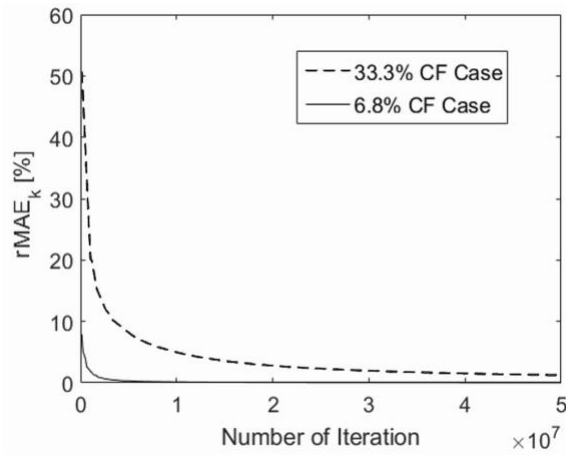
282 where  $k$  can also be replaced with GHI or PB. For  $k$ , the spatial averages (denoted by overbars) are over  
 283 all LES grid points. For GHI, the averages are over surface grid points in  $x$  and  $y$ . For PB, the averages are  
 284 over all pixels of all sky images.

285

286 **4. Results**

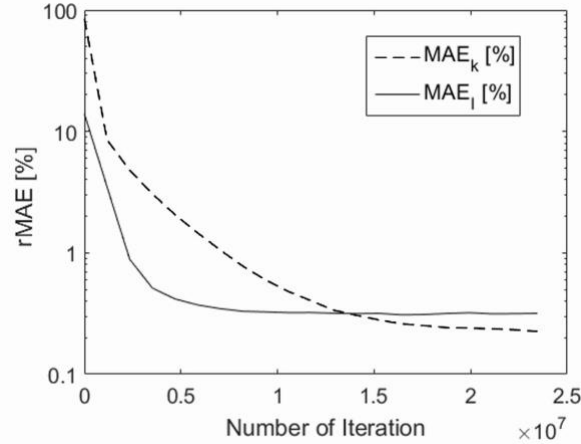
287 **4.1 Nine Imager Validation**

288 We validate the ART and iterative methods on the 9 imager deployment with a separation of 1.5 km against  
289 the ground truth  $k_{LES}$  for the two cloud fraction cases. A perfect  $\tau$  as defined in Eq. 12 is input to the ART.  
290 Figure 6 shows  $rMAE_k$  as a function of the number of iterations. The initial  $k$  guess results in a large  
291 reconstruction error, but the ART method decreases the  $k$  rMAE to 1.2% and 0.02% after  $5 \times 10^7$  iterations  
292 for a 33% and 6.8% cloud fraction (CF), respectively. The error for the high CF case continues to decrease  
293 after  $5 \times 10^7$  iterations while the low CF case converges to zero rMAE $_k$  after only  $1 \times 10^7$  iterations. Any  
294 additional cloud will block the view of other clouds in several imagers and limit the observability of cloud  
295 tops and clear sky grid points in the domain, requiring disproportionately more iterations to arrive at the  
296 solution. In the extreme case of an overcast cloud layer, cloud top heights could not be reconstructed at all.



297  
298 Figure 6. Convergence of ART as indicated by the relative mean absolute error of the extinction coefficients. 33.3% and 6.8% CF  
299 test cases are the dashed and solid lines, respectively.

300 Figure 7 validates the iterative reconstruction method. We input  $k$  output from the ART method. To validate  
301 the correct implementation of the iterative method, we eliminate the largest source of error by assuming  
302 that the source function  $J$  of the ground truth cloud field is known. Therefore referring to Figure 3 the  
303 gradient descent iteration loop is not required and only the constant source function iteration is executed.  
304 Figure 7 demonstrates that the iterative method converges to 0.2%  $k$  rMAE after  $2 \times 10^7$  iterations,  
305 significantly below the 1.2%  $k$  rMAE of the ART alone (Figure 6). The image rMAE converges faster, but  
306 remains slightly larger at 0.3%. However, each iteration with the iterative method takes significantly longer  
307 than an iteration with the ART method (see next section).



308

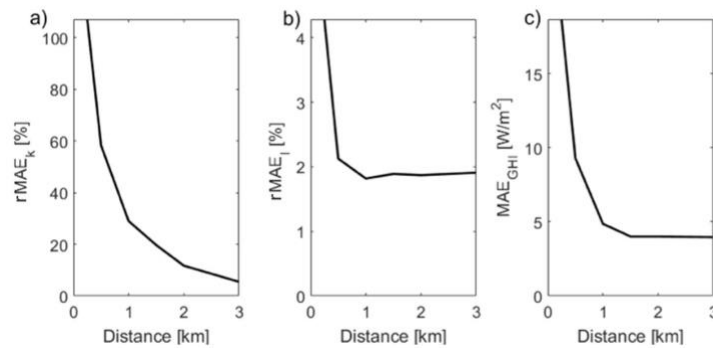
309 Figure 7. Convergence of iterative method  $k$  (dashed) and image (solid) relative mean absolute errors for the 33% CF case.

310 **4.2. Optimal Deployment**

311 **4.2.1. Optimal Sky Imager Distance**

312 The ART method is used to analyze optimal deployments because of its low computation cost. Using an  
 313 Intel Core i7-3770 3.4GHz computer, 9 imagers, and a cloud fraction of 2.3%, the ART method yields  
 314 converged results within about 30 seconds as opposed to 6 days with the iterative method, which  
 315 corresponds to a factor of  $2 \times 10^4$  difference in speed. The ART method (Section 3.1) is applied on a perfect  
 316  $\tau$  as defined in Eq. 12. Figure 8 shows that the accuracy of the retrieved  $k$  increases with distance between  
 317 imagers. GHI and image pixel brightness rMAE, on the other hand, do not improve for spacings larger than  
 318 1.5 km. The rMAE decreases the most between  $L = 0.25$  km and  $L = 0.5$  km.

319 The Appendix demonstrates the distance results for 4 and 2 imagers, respectively (Figure A1 and Figure  
 320 A2). The results for 4 imagers are consistent with Huang et al. (2008) who used the same number of imagers  
 321 with an optimum between  $2 \text{ km} < L < 4 \text{ km}$  for  $k$ . GHI and image rMAE perform worse as  $L$  increases  
 322 beyond 4 km. The 2-imager setup continues to improve with increased separation. Note that the optimal  
 323 sky imager distance is expected to scale with cloud height and possibly with other cloud geometrical  
 324 parameters, so the results should not be generalized.

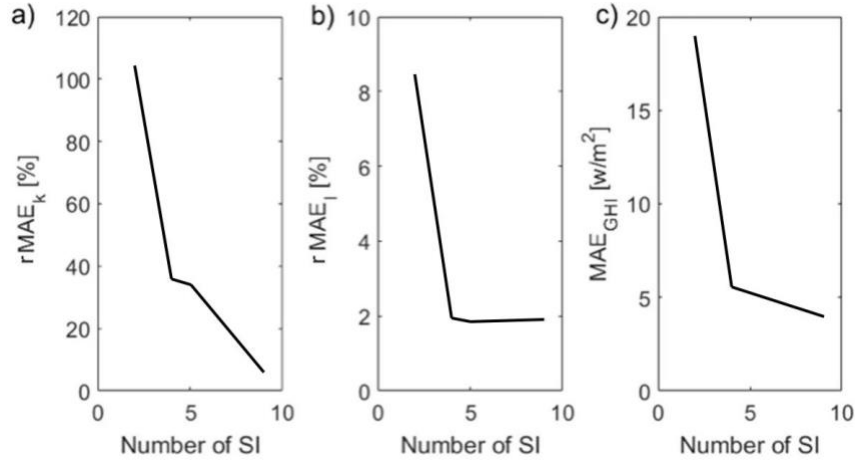


325

326 Figure 8. Domain averaged relative mean absolute error in (a)  $k$ , (b) image pixel brightness, and (c) Global Horizontal Irradiance  
 327 (GHI) for retrievals with 9 imagers at different distances  $L$  and for the 2.3% CF case.

328 **4.2.2. Optimal Number of Sky Imagers**

329 Figure 9 shows that increasing the number of SIs improves the overall reconstruction of the cloud domain.  
 330 Similar to Huang et al. (2008), we observe a large performance increase when using 4 imagers compared  
 331 to 2, and less improvement with additional imagers.

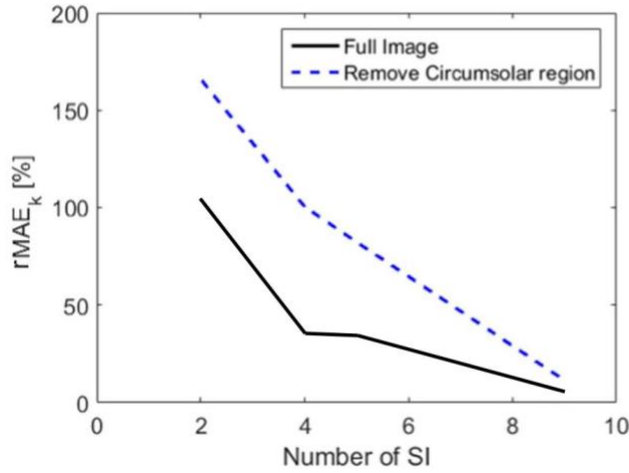


332  
 333 Figure 9. Domain averaged relative mean absolute error in (a) extinction coefficient  $k$ , (b) image pixel brightness, and (c) Global  
 334 Horizontal Irradiance (GHI) for retrievals with 2, 4, 5 and 9 imagers at their respective optimal separations and for the 2.3% CF  
 335 case.

336 Although improvements in GHI and image pixel rMAE between 4 and 9 imagers are minimal for an ideal  
 337 case, using 9 imagers improves the robustness of the cloud scene reconstruction in real applications. Two  
 338 mechanisms are expected to benefit tomographic methods applied to 4 or more imagers in real applications.  
 339 The first benefit is that dirt on the dome of one imager does not contaminate the results. In single-imager  
 340 cloud detection, dirt is often identified as a cloud since its red-blue-ratio is closer to clouds than the clear  
 341 sky. Reconstruction limits the impact of dirt because the only solution that can satisfy a “cloud” in one  
 342 image that is not present in any other images is a “cloud” located immediately above the imager. Such a  
 343 low ‘cloud’ would be invisible to the other imagers as data at large pixel zenith angles is poorly resolved  
 344 and therefore excluded. Thus, the constraint on minimum CBH results in the clearing of that cloud (see  
 345 Section 2.4).

346 The second benefit is that using data from the circumsolar region becomes unnecessary. As stated in Section  
 347 3.1, the circumsolar region in the sky hemisphere is a common source of cloud identification error. With 9  
 348 imagers, it is possible to ignore the circumsolar region in every imager as the neighboring imagers are able  
 349 to fill in the missing data for the circumsolar region. Figure 9a and Figure 10 demonstrate that in an ideal  
 350 case (no circumsolar region errors), the  $k$  MAE only decreases to 5% from 35%. Removing the pixels with  
 351 less than a 30 degree solar pixel angle (also referred to as scattering angle) in each image (Figure 10), the  
 352  $k$  MAE decreases to 15% from 80%, i.e. a much larger improvement in percentage points for 9 imagers

353 compared to 5 or fewer imagers. This result suggests that for real deployments at least 9 imagers are  
 354 recommended.



355  
 356 Figure 10. Domain averaged  $k$  rMAE for retrievals with 2, 4, 5 and 9 imagers using the full image (same as Figure 9a) in black and  
 357 removing the circumsolar region with solar pixel angle  $\theta_s < 30^\circ$  in each image in dashed blue.

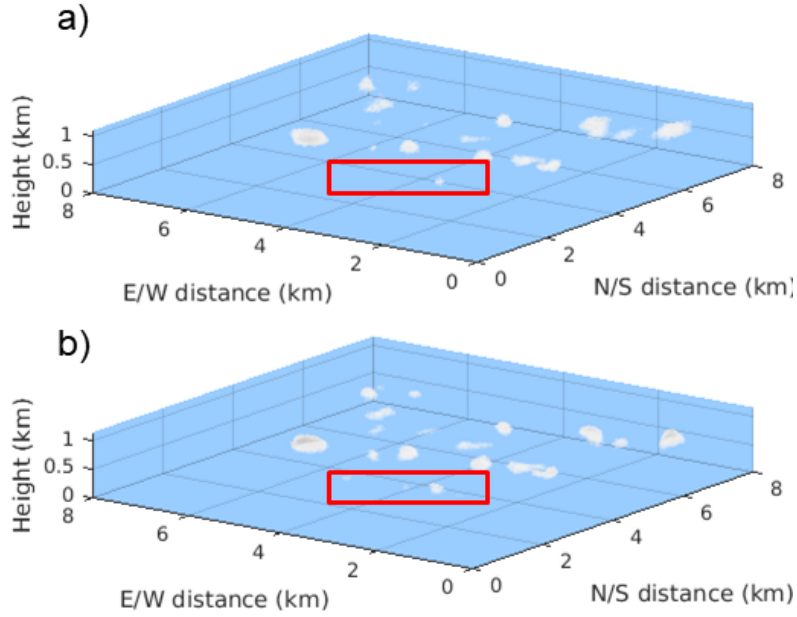
### 358 4.3. 3D Reconstruction Methods

359 To isolate characteristics of the reconstruction methods, we now focus on a specific deployment with 9  
 360 imagers spaced at  $L = 1.5$  km. We use 9 imagers because this is the optimum scenario to demonstrate the  
 361 limitations of the methods and not the deployments, while maintaining  $L = 1.5$  km (versus  $L = 3$  km) since  
 362 it becomes increasingly difficult to obtain permissions to install camera systems away from the location of  
 363 interest. For example, at a utility scale power plant with a typical dimension of  $2 \times 2$  km,  $L = 3$  km would  
 364 require obtaining permissions from up to 8 adjacent property owners.

#### 365 4.3.1. Algebraic Reconstruction Technique

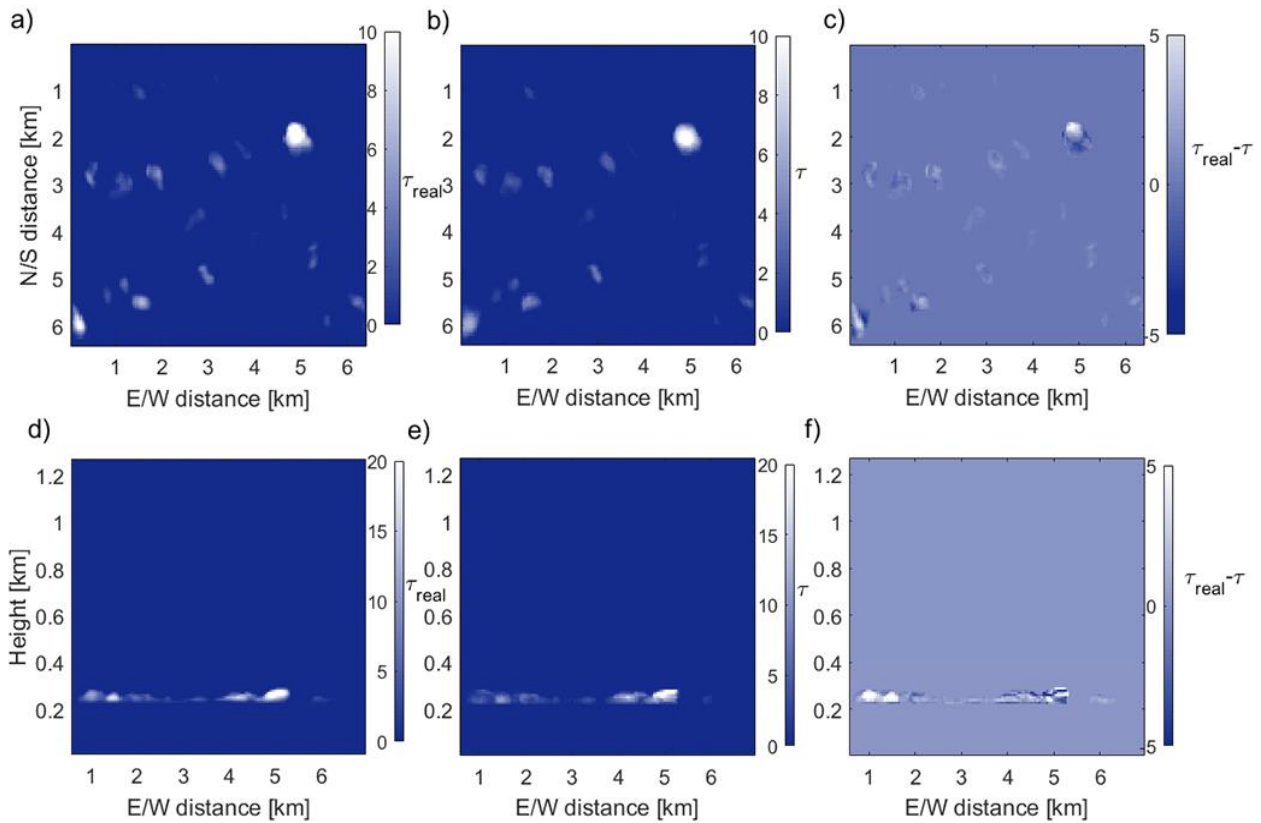
366 As described in Section 2.2, the ART method requires an input  $\tau$  to calculate  $k$ . Unlike in Section 4.1 where  
 367 the  $\tau$  input was assumed to be error-free based on Eq. 12, here the RRBR method provides the initial  $\tau$   
 368 (Mejia et al., 2016). The RRBR method uses both radiance and red blue ratio values to estimate  $\tau$  based on  
 369 a look-up table of SHDOM simulations of homogenous clouds. Since the RRBR is based on homogeneous  
 370 clouds, it has a propensity to underestimate  $\tau$  because homogeneous clouds are darker than heterogeneous  
 371 clouds on average. This underestimation in  $\tau$  is seen in Figure 11 and Table 1 as the  $k$  rMBE is +17.1%.  
 372 Figure 11 shows that the spatial distribution and size of clouds from the ART method correspond broadly  
 373 with the ground truth, but small differences in location and size cause a rMAE for  $k$  of 53.4% while the  
 374 GHI rMAE is significantly smaller at 1.53%.





375

376 Figure 11. 3-D depiction of reconstructed  $k$  from the Algebraic Reconstruction Technique (ART) (a) and ground truth (b). The red  
 377 boxes highlight an area where the extinction coefficients are underestimated by the ART method.



378

379 Figure 12. Vertical sum (a, b, and c) and North-South sum (d, e, and f) of  $k$  (equivalent to  $\tau$ ) for CF of 6.8% from LES (ground  
 380 truth; a and d); reconstructed from Algebraic Reconstruction Technique (ART; b and e); and their difference (c and f). North (N)  
 381 is up and East (E) is to the right per convention.

382 Table 1. Error statistics of Algebraic Reconstruction Technique (ART) and iterative method for a CF of 6.8%. rMAE [%] is the  
 383 relative mean absolute error, and rMBE [%] is the relative mean bias error. DNI is the Direct Normal Irradiance and GHI is the  
 384 Global Horizontal Irradiance.  $k$  is the extinction coefficient and  $\tau$  is the vertical sum of  $k$ . For  $k$ , the spatial averages (denoted by  
 385 overbars) are over all LES grid points. For GHI, the averages are over surface grid points in x and y. For PB, the averages are over  
 386 all pixels of all sky images.

	ART			Iterative method		
	rMAE [%]	MAE	rMBE [%]	rMAE [%]	MAE	rMBE [%]
$\tau$	34.80	0.0481 [-]	17.10	17.20	0.0238 [-]	2.80
$k$	53.40	0.00025 [-]	17.10	33.60	0.00015 [-]	2.80
GHI	1.53	10.10 W m <sup>-2</sup>	0.04	0.85	5.6 W m <sup>-2</sup>	-0.12
GHI (GHI / GHI <sub>clear</sub> < 0.98)	21.80	68.90 W m <sup>-2</sup>	-14.20	0.86	2.70 W m <sup>-2</sup>	-0.15
DNI	1.30	10.50 W m <sup>-2</sup>	-0.46	0.81	6.50 W m <sup>-2</sup>	-0.21
Image pixel red channel	4.30	-	1.30	0.70	-	0.60

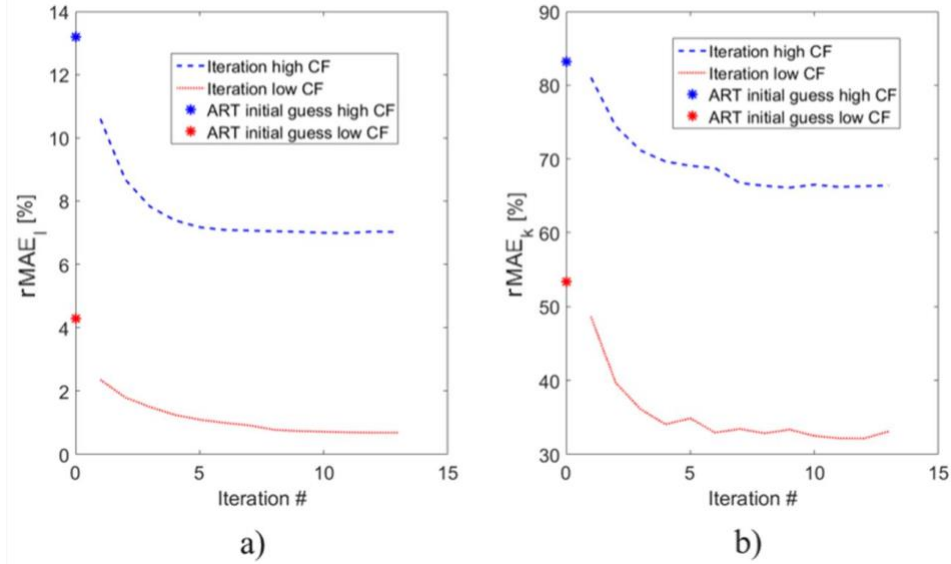
387  
 388 Since we expect the GHI error metrics to correlate with the number of cloudy pixels, Table 1 also shows  
 389 the GHI error metrics for cloud pixels only. For cloudy pixels (defined as GHI / GHI<sub>clear</sub> < 0.98) the rMAE  
 390 of GHI increases to 21.8% from 1.5% for all pixels. Most grid points are correctly identified, with 98.8%  
 391 of  $k$  being correctly separated as  $k = 0$  or  $k \neq 0$  (Table 2); same holds for cloudy grid points with 86% (=   
 392 4.8% / 5.6% ) being correctly identified.  $k$  grid points that are misidentified are either thin clouds ( $\tau < 0.5$ ),  
 393 e.g. in the north west of the domain (as seen in Figure 11 inside the red box) or at the edges of clouds.

394 Table 2. Contingency table of observed extinction coefficient and reconstructed Algebraic Reconstruction Technique (ART)  
 395 extinction coefficient,  $k$  for CF = 6.8%.

		Observation	
		$k = 0$	$k \neq 0$
ART	$k = 0$	94.0%	0.8%
	$k \neq 0$	0.4%	4.8%

### 396 4.3.2. Iterative Retrieval

397 The iterative method is based on the assumption that iteratively minimizing the image error further  
 398 minimizes the extinction coefficient errors. To decrease the computational cost,  $k$  from the ART method is  
 399 input to the iterative method as first guess. Unlike in Section 4.1 the source function is not assumed to be  
 400 known. Therefore the full bi-level iteration presented in Figure 3 is executed. Figure 13 and Table 1  
 401 demonstrate that the iterative method further decreases the image error. After 13 iterations, the image rMAE  
 402 decreases from 4.3% to 0.7% and 13.2% to 7.0% for the 6.8% and 33.3% CF cases, respectively. The  $k$   
 403 rMAE also decreases from 53.4% to 33.6% and 83.2% to 66.4% for the 6.8% and 33.3% CF cases,  
 404 respectively. For the small CF case  $k$  rMAE decreases nearly 20 percentage points, or 36%. The over-  
 405 predictive tendencies are resolved with the  $k$  rMBE improving from 17.1% to 2.8%, the GHI rMAE of  
 406 cloudy regions improving from 21.8% to 0.85%, and the GHI rMBE of cloudy regions improving from  
 407 14.2% to 0.15%.



408

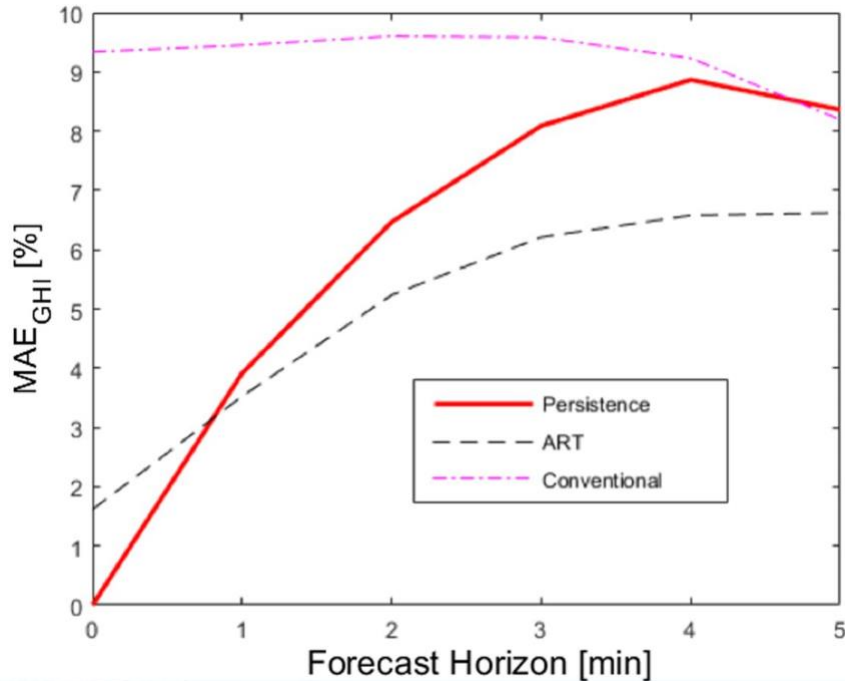
409 Figure 13. Mean average error for each iteration for the iterative method. a) Image pixel brightness; b) extinction coefficient.

#### 410 4.4. Solar Forecasting

411 Table 1 demonstrates that the rMAE in GHI is minor compared to the error in  $k$  for both the ART and the  
 412 iterative method. In this section only the ART method is considered as the iterative method is  
 413 computationally too expensive for operational forecasting. For atmospheric science applications, the  $k$   
 414 error magnitude indicates that the current methods require further improvements to provide high quality 3-D  
 415 cloud reconstructions. For solar energy applications, since surface GHI is the relevant quantity, and spatial  
 416 averages of GHI (over the area of the power plant) are more important than point-by-point quantities, the  
 417 ART method appears to be sufficient.

418 To demonstrate the potential of the ART for solar forecasting applications, the GHI map from the ART  
 419 method in section 4.2 is advected using the average cloud speed from the LES. This new method (“ART”)  
 420 is benchmarked against a naïve predictor (persistence; GHI remains identical to its value at forecast issue  
 421 time) and against the current conventional forecasts from a single sky imager. The single sky imager  
 422 forecast method is identical to Yang et al. (2014): the imager is located at the center of the domain, clouds  
 423 are represented in 2-D at the cloud height, and cloud optical depth is represented through a trinary (clear,  
 424 thin cloud, thick cloud) cloud decision.

425 Figure 14 demonstrates rMAE of persistence, conventional single sky imager, and the ART forecasts  
 426 relative to the ground truth measurements from the LES. The ART method significantly improves upon the  
 427 conventional method throughout the 5-minute forecast horizon. The improvements are due to better  
 428 representation of 3-D clouds as well as the more accurate representation of cloud optical depth compared  
 429 to the trinary system. At longer forecast times, the clouds evolve in shape and thickness, literally blurring  
 430 the advantage of better initial cloud conditions, and the ART forecast accuracy converges to the  
 431 conventional forecast. The accuracy of persistence forecasts decreases with forecast horizon for that same  
 432 reason. For forecast horizons of 1 to 5 min, the ART rMAE then beats persistence.



433

434 Figure 14. Global Horizontal Irradiance (GHI) forecast relative mean average error (MAE) for persistence forecast in red,  
 435 conventional single sky imager forecast (Yang et al., 2014) in magenta (dot-dashed), and Algebraic Reconstruction Technique  
 436 (ART) forecast in black (dashed). The persistence forecast assumes that the current GHI persists for the next 5 minutes.

## 437 5. Discussion and Conclusions

438 This paper introduces the application of tomographic methods to multiple sky images to reconstruct 3-D  
 439 fields of extinction coefficients. Virtual images are created by simulating 3-D heterogeneous cloud scenes  
 440 in the atmospheric boundary layer using LES. As expected, more imagers increase the accuracy of 3-D  
 441 cloud reconstruction, especially for up to 4 imagers after which the benefits of additional imagers decrease.  
 442 However, more imagers increase robustness to imager soiling and cloud detection errors in the circumsolar  
 443 region of images. Although having more imagers improves the accuracy of the 3-D reconstruction, it also  
 444 increases the capital, operations and maintenance cost of the imagers, creating a tradeoff between more  
 445 imagers and improved accuracy. The distance between imagers also plays an important role in  
 446 reconstruction accuracy. In idealized scenarios with a 0.94 km cloud base height, an increase in separation  
 447 between imagers led to an increase in 3-D reconstruction accuracy up to 3 km. This is because a diversity  
 448 in view perspectives better constrains cloud dimensions.

449 Summary statistics of the ART and the iterative methods are presented in Table 1. The  $k$  rMAE is 53.4%  
 450 using the ART and decreases to 33.6% after 13 iterations of the iterative method. The ART method, using  
 451  $\tau$  from the RRBR method, inherits the cloud optical depth under-predicting tendency of the RRBR as  
 452 demonstrated by the -17.1% rMBE of  $k$ . Although the iterative method decreases the rMBE, the  
 453 computational cost of several days to reconstruct a single cloud scene renders the method unusable for solar  
 454 forecast applications. Computational costs increase with higher cloud fraction as more cloud grid points  
 455 must be solved. On the other hand, the ART method takes only about 30 seconds, which is compatible with  
 456 solar forecast application. The ART method beats persistence forecast already at a 1-minute forecast  
 457 horizon, demonstrating its potential for solar energy applications.

458 It is important to note that these conclusions are for an idealized image and the results need to be validated  
459 in real images as well to account for both topographic obstructions and non-ideal lens distortion. Since  
460 buildings and trees commonly obstruct the horizon in an image, imagers where the cloud appears at a large  
461 zenith angle (near the horizon) may not contribute to the reconstruction of that cloud. Furthermore, cases  
462 with clouds obstructed by other clouds as in multiple cloud layers need to be investigated. Further, the  
463 sensitivity of the reconstruction accuracy to the surface albedo should be established given the abundant  
464 installation of utility-scale solar power plants near more reflective arid and semi-arid surfaces.

#### 465 **Acknowledgements**

466 We acknowledge funding from the California Energy Commission EPIC program. Felipe Mejia was  
467 supported by the National Science Foundation Graduate Research Fellowship under Grant No. (DGE-  
468 1144086). In addition, Íñigo de la Parra has been partially supported by the Spanish State Research Agency  
469 (AEI) and FEDER-UE under grants DPI2016-80641-R and DPI2016-80642-R.  
470

471 **References**

- 472 Aides, A., Schechner, Y.Y., Holodovsky, V., Garay, M.J., Davis, A.B., 2013. Multi sky-view 3D aerosol  
473 distribution recovery. *Opt. Express* 21, 25820. doi:10.1364/OE.21.025820
- 474 Chow, C.W., Belongie, S., Kleissl, J., 2015. Cloud motion and stability estimation for intra-hour solar  
475 forecasting. *Sol. Energy* 115, 645–655. doi:10.1016/j.solener.2015.03.030
- 476 Chow, C.W., Urquhart, B., Lave, M., Dominguez, A., Kleissl, J., Shields, J., Washom, B., 2011. Intra-  
477 hour forecasting with a total sky imager at the UC San Diego solar energy testbed. *Sol. Energy* 85,  
478 2881–2893. doi:10.1016/j.solener.2011.08.025
- 479 Evans, F., 2015. Spherical Harmonic Discrete Ordinate Method (SHDOM) radiative transfer model  
480 [WWW Document]. Accessed 2018-06-08. URL <http://nit.colorado.edu/shdom/shdomdoc/>  
481 (accessed 6.8.18).
- 482 Evans, K.F., 1998. The Spherical Harmonics Discrete Ordinate Method for Three-Dimensional  
483 Atmospheric Radiative Transfer. *J. Atmos. Sci.* 55, 429–446. doi:10.1175/1520-  
484 0469(1998)055<0429:TSHDOM>2.0.CO;2
- 485 Gordon, R., Bender, R., Herman, G.T., 1970. Algebraic reconstruction techniques (ART) for three-  
486 dimensional electron microscopy and x-ray photography. *J. Theor. Biol.* 29, 471–481.  
487 doi:10.1016/0022-5193(70)90109-8
- 488 Hammer, A., Heinemann, D., Westerhellweg, A., 1999. Daylight and solar irradiance data derived from  
489 satellite observations - The satellight project, in: *Proc. EUMETSAT Meteorological Satellite Data*  
490 *Users Conference*. pp. 331–337.
- 491 Holben, B.N., Eck, T.F., Slutsker, I., Tanré, D., Buis, J.P., Setzer, A., Vermote, E., Reagan, J.A.,  
492 Kaufman, Y.J., Nakajima, T., Lavenu, F., Jankowiak, I., Smirnov, A., 1998. AERONET—A  
493 Federated Instrument Network and Data Archive for Aerosol Characterization. *Remote Sens.*  
494 *Environ.* 66, 1–16. doi:10.1016/S0034-4257(98)00031-5
- 495 Holodovsky, V., Schechner, Y.Y., Levin, A., Levis, A., Aides, A., 2016. In-situ multi-view multi-  
496 scattering stochastic tomography. 2016 IEEE Int. Conf. Comput. Photogr. ICCP 2016 - Proc.  
497 doi:10.1109/ICCPHOT.2016.7492869
- 498 Huang, D., Liu, Y., Wiscombe, W., 2008. Determination of cloud liquid water distribution using 3D  
499 cloud tomography. *J. Geophys. Res. Atmos.* 113, 1–13. doi:10.1029/2007JD009133
- 500 Kurtz, B., Mejia, F., Kleissl, J., 2017. A virtual sky imager testbed for solar energy forecasting. *Sol.*  
501 *Energy* 158, 753–759. doi:10.1016/j.solener.2017.10.036
- 502 Levis, A., Schechner, Y.Y., Aides, A., Davis, A.B., 2015. Airborne three-dimensional cloud tomography.  
503 *Proc. IEEE Int. Conf. Comput. Vis. 2015 Inter*, 3379–3387. doi:10.1109/ICCV.2015.386
- 504 Levis, A., Schechner, Y.Y., Davis, A.B., 2017. Multiple-Scattering Microphysics Tomography, in: *The*  
505 *IEEE Conference on Computer Vision and Pattern Recognition (CVPR)*. pp. 6740–6749.
- 506 Lorenz, E., Remund, J., Müller, S.C., Traunmüller, W., Steinmaurer, G., Pozo, D., Ruiz-Arias, J.A.,  
507 Fanego, V.L., Ramirez, L., Romeo, M.G., Kurz, C., Pomares, L.M., Guerrero, C.G., 2009.  
508 Benchmarking of Different Approaches to Forecast Solar Irradiance, in: *24th European Photovoltaic*  
509 *Solar Energy Conference*. pp. 4199–4208.

- 510 Markham, B.L., 1992. Surface Reflectance Retrieval From Satellite and Aircraft Results of Sensor and  
511 Algorithm Comparisons During FIFE. *J. Geophys. Res.* 97, 18,785-18,795.
- 512 Martín, A., Trapero, J.R., 2015. Recursive Estimation Methods to Forecast Short-Term Solar Irradiation,  
513 in: Lefebvre G., Jiménez E., Cabañas B. (Eds) *Environment, Energy and Climate Change II. The*  
514 *Handbook of Environmental Chemistry*, Vol 34. Springer, Cham. pp. 41–53. doi:10.1007/698
- 515 Mathiesen, P., Collier, C., Kleissl, J., 2013. A high-resolution, cloud-assimilating numerical weather  
516 prediction model for solar irradiance forecasting 92, 47–61. doi:10.1016/j.solener.2013.02.018
- 517 Mathiesen, P., Kleissl, J., 2011. Evaluation of numerical weather prediction for intra-day solar forecasting  
518 in the continental United States. *Sol. Energy* 85, 967–977. doi:10.1016/j.solener.2011.02.013
- 519 Mejia, F.A., Kurtz, B., Murray, K., Hinkelman, L.M., Sengupta, M., Xie, Y., Kleissl, J., 2016. Coupling  
520 sky images with radiative transfer models: A new method to estimate cloud optical depth. *Atmos.*  
521 *Meas. Tech.* 9, 4151–4165. doi:10.5194/amt-9-4151-2016
- 522 Min, Q.-L., 2003. Validation of surface retrieved cloud optical properties with in situ measurements at the  
523 Atmospheric Radiation Measurement Program (ARM) South Great Plains site. *J. Geophys. Res.*  
524 108, 4547. doi:10.1029/2003JD003385
- 525 Miyamoto, K., 1964. Fish Eye Lens. *J. Opt. Soc. Am.* 54, 1060. doi:10.1364/JOSA.54.001060
- 526 Nguyen, D., Kleissl, J., 2014. Stereographic methods for cloud base height determination using two sky  
527 imagers. *Sol. Energy* 107, 495–509. doi:10.1016/j.solener.2014.05.005
- 528 Oberländer, J., Pfozter, L., Roennau, A., Dillmann, R., 2015. Fast calibration of rotating and swivelling 3-  
529 D laser scanners exploiting measurement redundancies. *IEEE Int. Conf. Intell. Robot. Syst.*  
530 doi:10.1109/IROS.2015.7353796
- 531 Peng, Z., Yu, D., Huang, D., Heiser, J., Yoo, S., Kalb, P., 2015. 3D cloud detection and tracking system  
532 for solar forecast using multiple sky imagers. *Sol. Energy* 118, 496–519.  
533 doi:10.1016/j.solener.2015.05.037
- 534 Quesada-Ruiz, S., Chu, Y., Tovar-Pescador, J., Pedro, H.T.C., Coimbra, C.F.M., 2014. Cloud-tracking  
535 methodology for intra-hour DNI forecasting. *Sol. Energy* 102, 267–275.  
536 doi:10.1016/j.solener.2014.01.030
- 537 Schmidt, T., Kalisch, J., Lorenz, E., Heinemann, D., 2015. Evaluating the spatio-temporal performance of  
538 sky imager based solar irradiance analysis and forecasts. *Atmos. Chem. Phys. Discuss.* 15, 26997–  
539 27039. doi:10.5194/acpd-15-26997-2015
- 540 Seeram, E., 2015. Chapter 3: Physical Principles of CT, in: *Computed Tomography 4th Edition Physical*  
541 *Principles, Clinical Applications, and Quality Control.* p. 576.
- 542 Stevens, B., 2010. Introduction to UCLA-LES [WWW Document]. Accessed 2018-06-08.  
543 doi:10.1007/978-1-4419-6169-3
- 544 Sun, X.J., Li, H.R., Barker, H.W., Zhang, R.W., Zhou, Y.B., Liu, L., 2016. Satellite-based estimation of  
545 cloud-base heights using constrained spectral radiance matching. *Q. J. R. Meteorol. Soc.* 142, 224–  
546 232. doi:10.1002/qj.2647
- 547 Urquhart, B., Ghonima, M., Nguyen, D.A., Kurtz, B., 2013. Sky-Imaging Systems for Short-Term  
548 Forecasting, in: *Solar Energy Forecasting and Resource Assessment.* pp. 195–232.

549           doi:10.1016/B978-0-12-397177-7.00009-7

550   Urquhart, B., Kurtz, B., Dahlin, E., Ghonima, M., Shields, J.E., Kleissl, J., 2015. Development of a sky  
551       imaging system for short-term solar power forecasting. *Atmos. Meas. Tech.* 8, 875–890.  
552       doi:10.5194/amt-8-875-2015

553   Urquhart, B., Kurtz, B., Kleissl, J., 2016. Sky camera geometric calibration using solar observations.  
554       *Atmos. Meas. Tech.* 9, 4279–4294. doi:10.5194/amt-9-4279-2016

555   Veikherman, D., Aides, A., Schechner, Y.Y., Levis, A., 2015. Clouds in the cloud. *Lect. Notes Comput.*  
556       *Sci. (including Subser. Lect. Notes Artif. Intell. Lect. Notes Bioinformatics)* 9006, 659–674.  
557       doi:10.1007/978-3-319-16817-3\_43

558   Wang, G., Kurtz, B., Kleissl, J., 2016. Cloud base height from sky imager and cloud speed sensor. *Sol.*  
559       *Energy* 131, 208–221. doi:10.1016/j.solener.2016.02.027

560   Wu, X., Jin, S., Li, Y., Dong, Y., 2017. Voxel Nodes Model Parameterization for GPS Water Vapor  
561       Tomography, in: Sun J., Liu J., Yang Y., Fan S., Yu W. (Eds) *China Satellite Navigation*  
562       *Conference (CSNC) 2017 Proceedings: Volume I. CSNC 2017. Lecture Notes in Electrical*  
563       *Engineering, Vol 437.* Springer, Singapore. pp. 3–12. doi:10.1007/978-981-10-4588-2

564   Yang, H., Kurtz, B., Nguyen, D., Urquhart, B., Chow, C.W., Ghonima, M., Kleissl, J., 2014. Solar  
565       irradiance forecasting using a ground-based sky imager developed at UC San Diego 103, 502–524.

566   Ye, S., Xia, P., Cai, C., 2016. Optimization of GPS water vapor tomography technique with radiosonde  
567       and COSMIC historical data. *Ann. Geophys.* 34, 789–799. doi:10.5194/angeo-34-789-2016

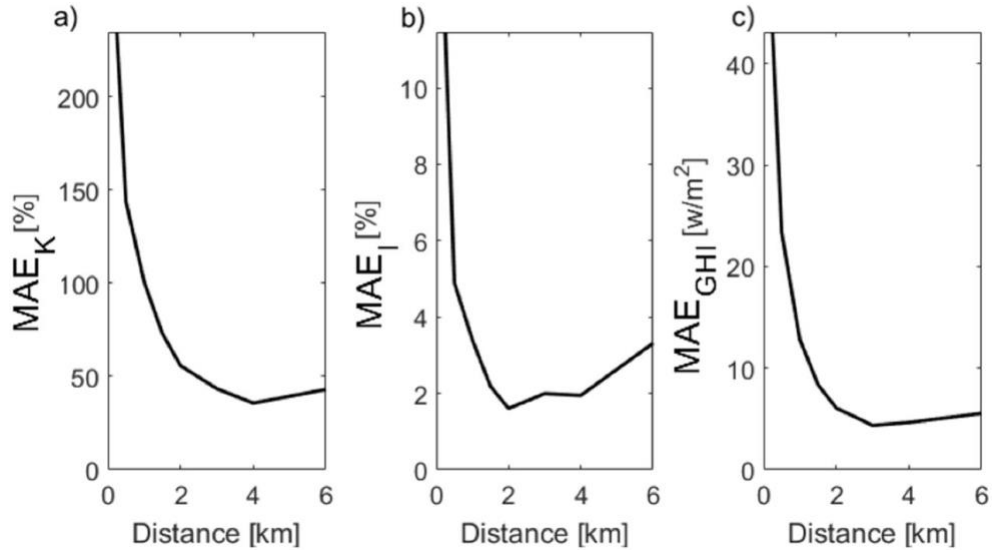
568   Zhong, X., Sahu, D.K., Kleissl, J., 2017. WRF inversion base height ensembles for simulating marine  
569       boundary layer stratocumulus. *Sol. Energy* 146, 50–64. doi:10.1016/j.solener.2017.02.021

570



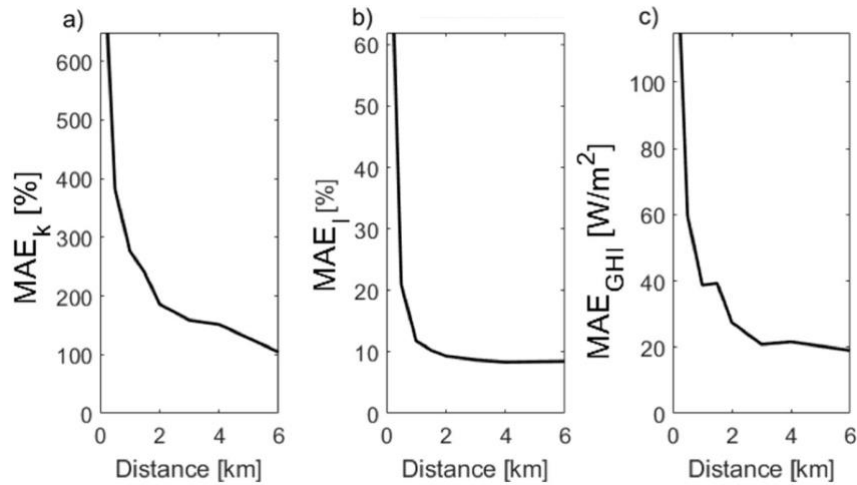
571 **Appendix**

572 Figure A1 and Figure A2 are the equivalent of Figure 8 and demonstrate the improvements with increased  
 573 separation for 4 and 2 imager deployments respectively. The results are consistent with Huang et al., (2008)  
 574 with an optimum between  $2 \text{ km} < L < 4 \text{ km}$  for  $k$ . GHI and image error perform worse as  $L$  increases beyond  
 575 4 km. The 2-imager setup continues to improve with increased separation.



576

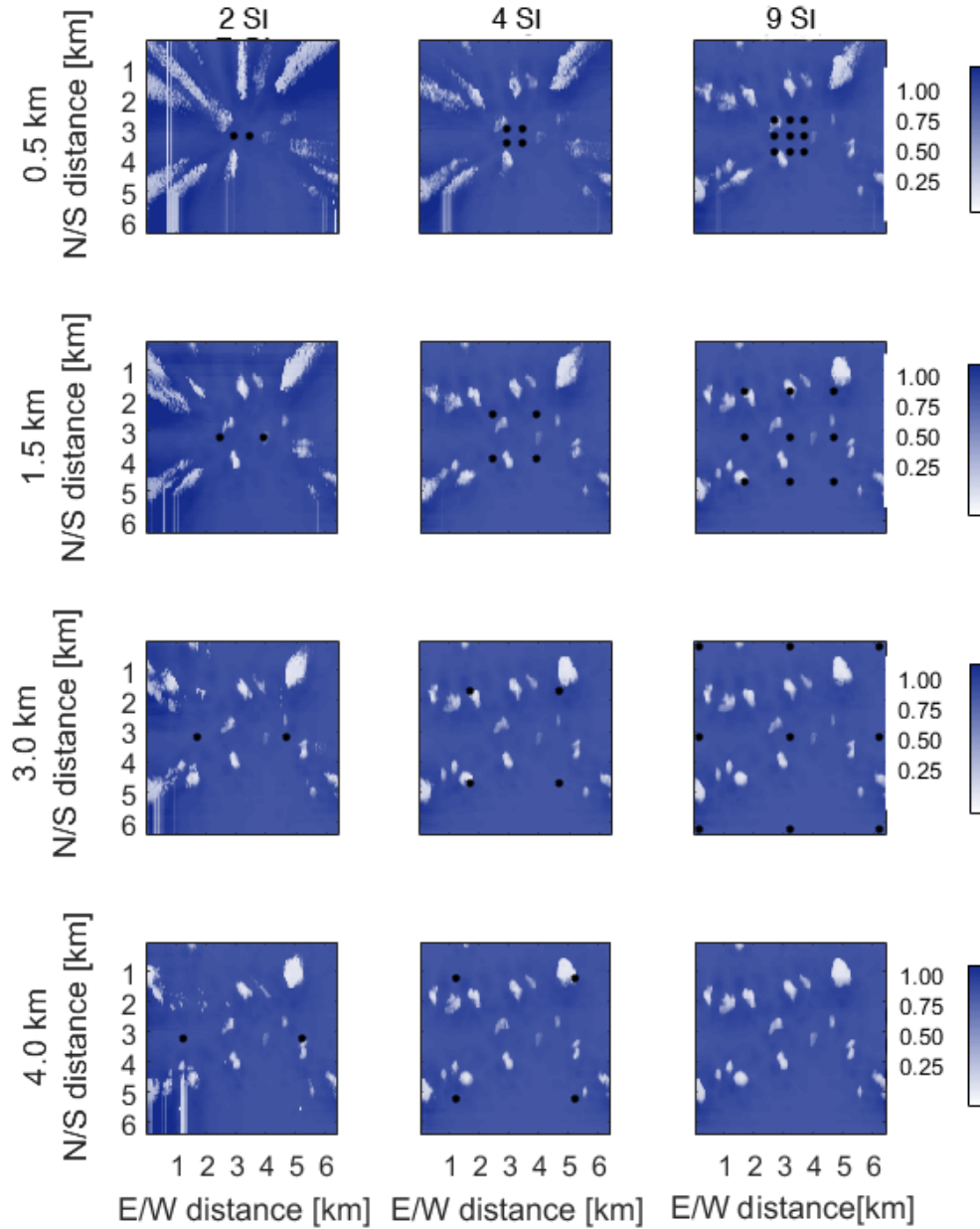
577 Figure A1. Domain averaged mean error in (a)  $k$ , (b) image pixel brightness, and (c) Global Horizontal Irradiance (GHI) for  
 578 retrievals with 4 imagers at different distances  $L$ .



579

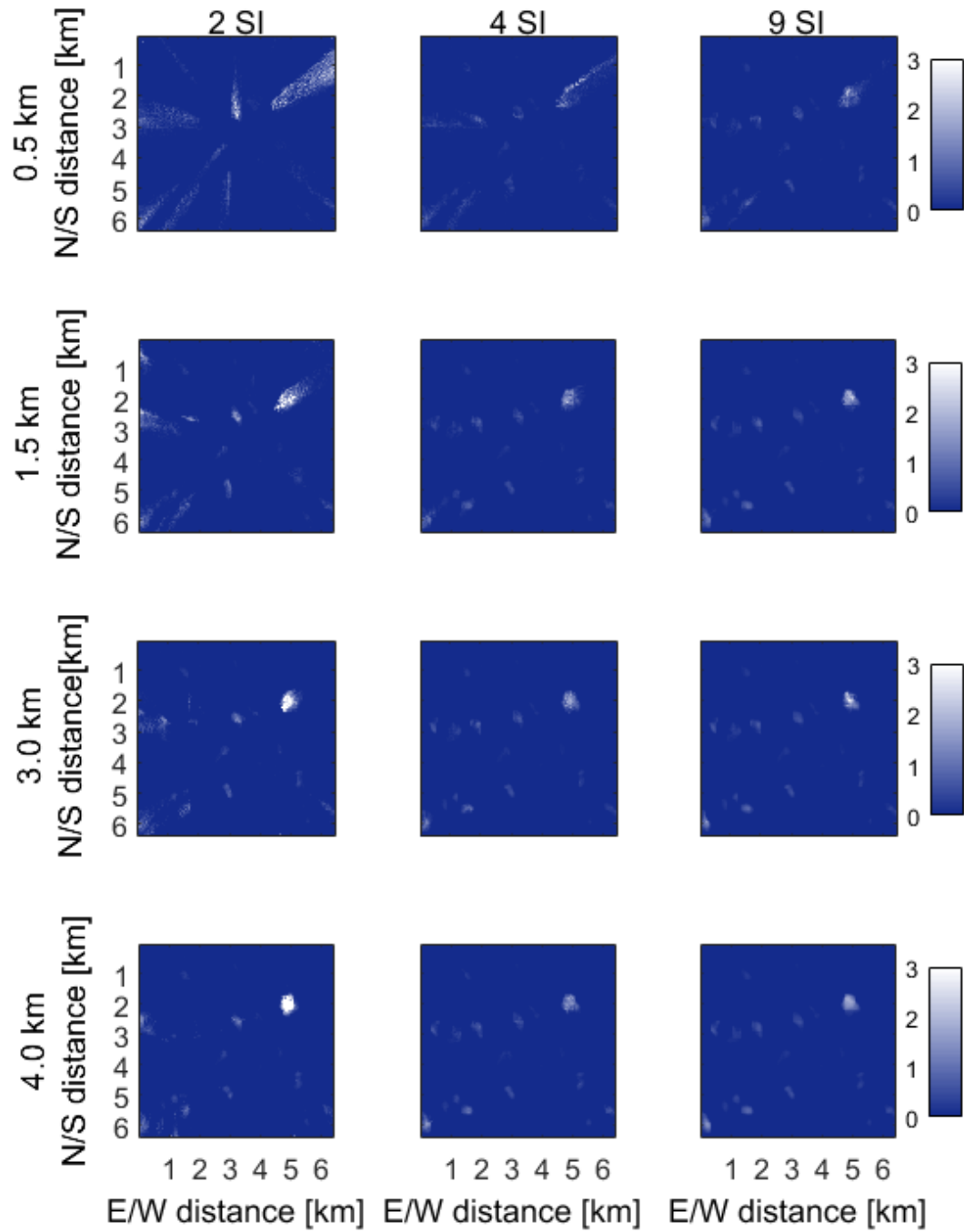
580 Figure A2. Domain averaged mean error in (a)  $k$ , (b) image pixel brightness, and (c) Global Horizontal Irradiance (GHI) for  
 581 retrievals with 2 imagers at different distances  $L$ .

582 Figure A3 through Figure A5 show the reconstructed spatial fields of clear sky index and two perspectives  
 583 of the extinction coefficient  $k$ . The results in Figure 8 are based on the data shown in these figures.



584

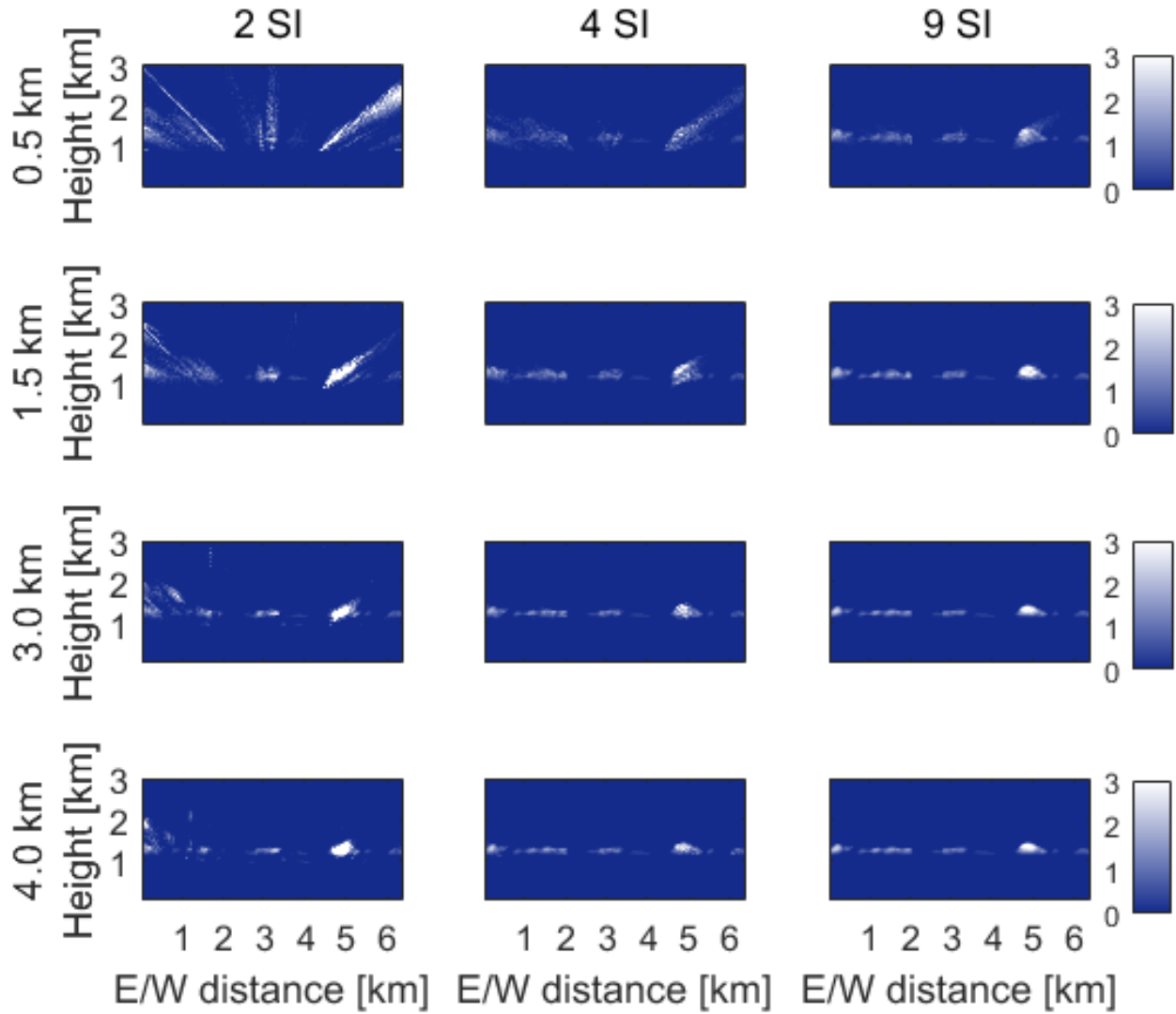
585 Figure A3. Spherical Harmonic Discrete Ordinate Method (SHDOM) simulated clear sky index at the surface from the  
 586 reconstructed extinction coefficient field from different numbers of imagers (columns) at different spacing  $L$  (rows) for a CF of  
 587 6.8% using the ART method. Black dots represent imager locations. The bottom right image is ground truth from Large Eddy  
 588 Simulation (LES).



589

590  
591

Figure A4. Reconstructed vertically averaged extinction coefficient  $k$  from different number of imagers (columns) at different spacings  $L$  (rows) for a CF of 6.8% using the ART method. The bottom right graph is the correct  $k$ .



592

593 Figure A5. Reconstructed extinction  $k$  averaged in the North-South direction from different numbers of imagers (columns) at  
 594 different spacings  $L$  (rows) for a CF of 6.8% using the ART method. The bottom right graph is the correct  $k$ . The data shown is  
 595 identical to Figure A4, but as a vertical slice rather than a top-down view.